

1  
2  
3  
4  
5  
6  
7  
8  
9  
10  
11  
12  
13  
14  
15  
16  
17  
18  
19  
20  
21  
22  
23  
24  
25  
26  
27  
28  
29  
30  
31  
32  
33  
34  
35  
36  
37  
38  
39  
40  
41

SUBMISSION TO  
COMPUTERS AND GEOTECHNICS

DATE:

Revised: July 2021

TITLE:

PLATYMATCH- A particle-matching algorithm for the analysis of platy particle kinematics using X-ray Computed Tomography

AUTHORS:

Christopher U. Ibeh

Matteo Pedrotti

Alessandro Tarantino

Rebecca J. Lunn

AFFILIATION:

Department of Civil and Environmental Engineering, University of Strathclyde, Glasgow, UK

CORRESPONDING AUTHOR:

Mr Cristopher Ibeh

Department of Civil and Environmental Engineering

University of Strathclyde

James Weir Building - Level 5

75 Montrose Street - Glasgow G1 1XJ, Scotland, UK

E-mail : christopher.ibeh@strath.ac.uk

KEYWORDS

PLATYMATCH, X-ray Computer tomography (X-CT), mica, clay, particle matching, algorithm

Number of words: 7791

Number of figures: 20

Number of tables: 3

42 **7: PLATYMATCH- A PARTICLE-MATCHING**  
43 **ALGORITHM FOR THE ANALYSIS OF PLATY**  
44 **PARTICLE KINEMATICS USING X-RAY COMPUTED**  
45 **TOMOGRAPHY**

46

47 **ABSTRACT**

48 Particle scale mechanisms influence the mechanical behaviour of geomaterials. A better  
49 understanding of soil micromechanics will help develop more accurate constitutive models  
50 and, by extension, safer and more economic geotechnical design. Sand-grained soils have been  
51 widely studied at the particle scale using X-ray Computed tomography and this has revealed  
52 important micromechanical behaviour of sands. Clays are least understood and studied at the  
53 particle scale. As technology rapidly progresses, to understand clay kinematics, a particle  
54 kinematic algorithm to match plate shaped (platy) particles will be required. Current algorithms  
55 developed for the matching of quartz and carbonate sand particles may not be suitable, since  
56 particle attributes that are strong discriminators of round particles may be less unique on platy  
57 particles, due to their extremely small c-axis and the reduced image resolution associated with  
58 their smaller size. This study presents, particle tracking of kaolin sample using mica markers  
59 and provides a platy soil particle matching algorithm for evaluating platy particle kinematics.  
60 After testing a range of alternative particle attributes, it was observed that a combination of  
61 particle major axis length, intermediate axis length, and perimeter was a good discriminant of  
62 the platy mica particles studied. On this basis, we developed PLATYMATCH, an optimised  
63 platy particle matching algorithm that considers a minimised combined normalised error of  
64 unique particle attributes within a defined search volume space. The algorithm was  
65 implemented such that particle attributes were compared in parallel, rather than sequentially,

66 to avoid filtering out a potential particle match based on a single non-unique attribute.

67 PLATYMATCH was then successfully validated using a compressed mica soil sample.

68

69

70 **Keywords:** PLATYMATCH, X-ray Computer tomography (X-CT), mica, clay, particle

71 matching, algorithm

72

73

## 74 1 INTRODUCTION

75 An increasing body of research shows that the particle scale properties of soil importantly  
76 influence the mechanical behaviour of granular materials. Sand-grained soils unlike clays have  
77 been widely studied at the particle scale and this has revealed important micromechanical  
78 behaviours including the change of sand grain morphology due to fracture mechanisms (Zhao  
79 et al. 2015), the decrease of dilatant behaviour with the suppression of peak shear strength in  
80 sand mixed with tyre chips (Chevalier et al. 2019), and the observation of pre-peak initiation  
81 of strain localisation in sand using X-ray computer tomography (X-ray CT) (Andò et al. 2012).  
82 Despite clay soils exhibiting relatively more complex behaviour compared to sands, clays are  
83 less understood and studied at the particle scale. This is because clay particles are very small –  
84 with size in the order of microns/sub-microns and thickness in the order of tenths/hundredths  
85 of nanometres, they are platy in shape, and they exhibit physico-chemical interactions in  
86 addition to mechanical interactions. An improved understanding of clay micromechanics could  
87 inform macroscopic constitutive models (Sridharan and Venkatappa Rao, 1973, Cetin et al.  
88 2007, Pedrotti and Tarantino, 2018, Pedrotti and Tarantino, 2019, Ibeh et al. 2019, Alonso et  
89 al. 2010, Hattab et al. 2010, Lin et al. 2021) enabling greater accuracy of predictions and, by  
90 extension, safer and more economic geotechnical design.

91 To better understand soil discrete mechanics, X-ray CT imaging techniques have been used to  
92 capture the particle scale attributes of soils subjected to different types of loading over time  
93 (mechanical, thermal, hydraulic, etc.). The X-ray CT data provides detailed 3D images of  
94 microscopically deformed geomaterials (Nielsen et al. 2003; Takamura et al. 2004; Viggiani et  
95 al. 2004; Haldrup et al. 2008; Taylor et al. 2015; Karatza et al 2019; Reijonen et al. 2020; and  
96 Chen et al. 2021. This technique could provide localized strain measurements). To determine  
97 particle motion, the analysis of such images usually requires particle matching between pre-  
98 and post-deformation scans, i.e. before and after loading. Two approaches are commonly used

99 for this analysis. Discrete digital image correlation - Discrete DIC (Hall et al. 2010; Ando et  
100 al. 2012) recognises grains based on their image (numerous voxel grey-scale information)  
101 which can be further analysed full field strain measurement with the main limitation of being  
102 computationally expensive (Ando et al. 2012). Alternatively, particle before and after loading  
103 are matched using simple morphological particle attributes. Even if only a fraction of particles  
104 is matched, this approach enables the effective determination of sample kinematics with the  
105 advantage of being less computationally expensive (Ando et al. 2012).

106 A summary of key particle matching approaches to-date for granular materials is presented in  
107 Table 1. Fu et al. (2008) implemented a particle matching algorithm to match crushed limestone  
108 particles (average size of  $127\mu\text{m}$ ), using expected particle position reference and volume as  
109 matching parameters. They assumed that the sample deformed as a continuum and hence the  
110 algorithm searches for a particle in the initial sample scan with the closest location to where  
111 the particle should be in the second scan 2 (after loading). They then used the particle volume  
112 as an additional parameter if there was more than one particle in that location. This search  
113 approach may, however, break-down when searching for particles in a shear band (where  
114 particles could move in an unpredictable manner). Ando et al. (2012) developed a particle  
115 matching algorithm -ID Track and used it to match carbonate and quartz sand (average size of  
116  $400\mu\text{m}$  and imaged at  $15\mu\text{m}$  voxel size). ID Track searches for particles in two passes with  
117 the first pass using only volume difference and the second pass using both volume difference  
118 and difference of displacement of neighbouring particles. Particles with the closest attribute to  
119 the one under consideration are matched. Their assumption is that grains will tend to displace  
120 like their neighbours but also noted that this may cause problems when a neighbourhood  
121 overlaps a developed shear band. They used only one particle attribute as a matching parameter,  
122 i.e. volume, which would clearly present a challenge for particles where the volume may be  
123 poorly variable. Cheng and Wang (2018) also implemented an algorithm similar to ID-Track

124 to match quartz sand with an average size of 500  $\mu\text{m}$  and imaged at 6.5  $\mu\text{m}$  voxel size, but  
 125 rather than using volume as the matching parameter, they used surface area instead producing  
 126 similar results. Druckrey & Alshibli (2014) implemented an algorithm to match quartz sand  
 127 particles with an average size of 700  $\mu\text{m}$  and 10.85  $\mu\text{m}$  voxel size that compared particles  
 128 between scans using multiple particle attributes: Volume (number of voxels included in the  
 129 particle), Area (Area of the object boundary), Feret length (the distance between two parallel  
 130 planes tangent to the particle on the maximum extent direction - maximum Feret diameter),  
 131 and Feret width (the distance between two parallel planes tangent to the particle on the  
 132 minimum extent direction -minimum Feret diameter). These attributes were considered in  
 133 series (sequentially), and as such, a particle must be within a set tolerance for the first attribute  
 134 to be considered using the second, then similarly for the third and fourth. Table 1 presents  
 135 details of the samples studied, the imaging condition and the algorithm implementation  
 136 approach used. The table also contains details of the sample studied and the particle matching  
 137 algorithm implemented.

138

139 *Table 1: available matching algorithm and their implementation*

	Author	(Fu et al. 2008)	(Andò et al. 2012)	(Druckrey & Alshibli, 2014)	(Cheng & Wang, 2018)	This Study
1	Material and size	Crushed Limestone	Calcareous and quarzitic Sand	Quarzitic sand	Sand	Mica
2	Sample-size (Diameter X Height)	103 mm X 100 mm	11mm X 22 mm	19.5mm X 20.2mm	8mm X 16 mm	10mm X 20mm
3	Average Particle size	127 $\mu\text{m}$	400 $\mu\text{m}$	700 $\mu\text{m}$	500 $\mu\text{m}$	70 $\mu\text{m}$
4	Voxel size	-	15 $\mu\text{m}$	10.85 $\mu\text{m}$	6.5 $\mu\text{m}$	10 $\mu\text{m}$
5	Average ratio of particle major axis to voxel size		27	65	77	7
6	Average ratio of particle minor axis to voxel size		27	65	77	1
7	Particle segmentation approach	-	Watershed segmentation	Watershed segmentation	-	Machine learning trainable Weka

8	Search box used	No	Yes	Yes	Yes	Yes
9	Particle attribute used for matching.	Particle proximity	Particle position and particle volume	Particle position with sequential filtering of particle attributes: Volume, Surface area; Feret width and Feret lengths	Particle position and particle Area or Volume	Particle position with normalised parallel filtering of particle attributes: Major and intermediate axis length and perimeter.
10	Matching criteria	Direct comparison	Iterative comparison	Sequential comparison	Iterative comparison	Parallel comparison

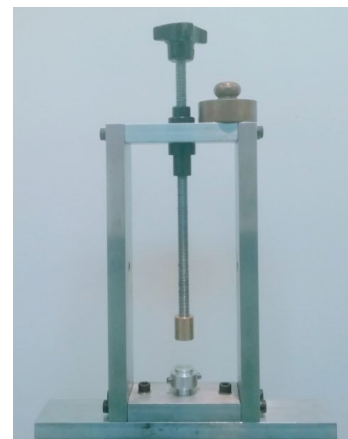
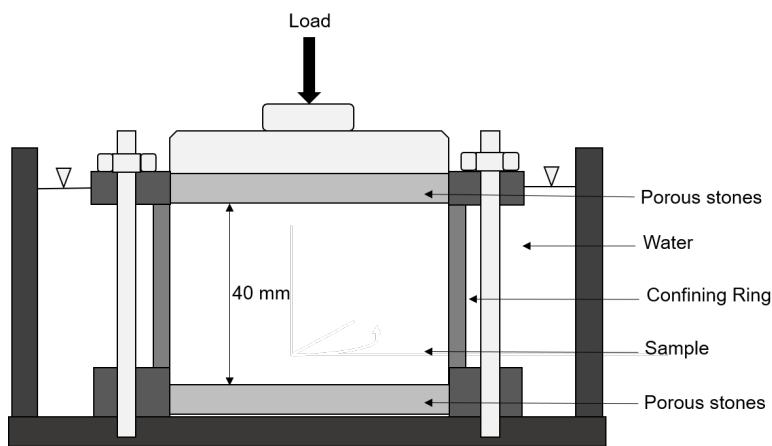
140

141 The aim of the research presented here is to understand how to match relatively small platy  
142 particles (mica silt) as a guide to better understanding clay particle kinematics. We studied this  
143 by first using the available matching algorithm by Druckrey and Alshibli, (2014) which was  
144 originally developed for matching sand round particles. Applying the algorithm, we observed  
145 some challenges due to the platy shape, lesser image resolution (as a result of the smaller  
146 particle size) and associated geometry peculiarities. We then developed and validated  
147 PLATYMATCH (available at <https://github.com/Christopher-Ibeh/PLATYMATCH>), an  
148 optimised platy particle matching algorithm, taking into consideration the lessons learnt from  
149 implementing the Druckrey and Alshibli, (2014) code. In the future, PLATYMATCH can be  
150 used to further the understanding of the kinematics of plate shaped particles. For the example  
151 presented here of tracking platy mica particles, embedded in clay, it could provide new  
152 information on the evolution of strain localisation, since unlike tracking round particles,  
153 tracking plate-shaped particles provides information on particle rotation, as well as particle  
154 displacement.

## 155 2 MATERIAL AND SAMPLE PREPARATION

156 We tested soil samples (mica silt) with a significantly smaller particle size to voxel size ratio  
157 compared to the samples tested by the works listed in table 1. The number of mica particles per  
158 unit volume was decreased by embedding the mica silt (1.5% by weight) in kaolin (98.5% by  
159 weight) to reduce any particle segmentation error that may emanate from particles sticking  
160 face-to-face.

161 Ground muscovite mica passing through sieve size 400-micron and Speswhite kaolin with a  
162 liquid limit (LL) of 0.64 and a plastic limit (PL) of 0.32, were used for the tests. The grain size  
163 distribution of the Kaolin shows it is composed of 80% clay-sized particles and 20% silt-sized  
164 particles. After mixing the appropriate amount of mica (1.5% by weight) and kaolin (98.5% by  
165 weight) with de-aired distilled water using 1.5 times the liquid limit of kaolin (96%), the  
166 resultant slurry was consolidated in a modified oedometer cell (40mm ring height see figure  
167 1a) to 2200kpa, then unloaded under drained conditions to 200kpa and finally quickly unloaded  
168 (quasi-undrained unloading). This procedure was adopted to create overconsolidated samples  
169 (OCR=11). When unloading the sample, the last 200 kPa were unloaded under undrained  
170 conditions to generate suction and hence some apparent cohesion and facilitate the trimming  
171 of the specimen. Samples were trimmed to 20mm height and 10mm diameter using a miniature  
172 soil lathe (see figure 1b). After preparing the lathe-trimmed specimen, the specimen was  
173 covered with a cling film to minimise moisture loss during imaging.



(a)

(b)

176 *Figure 1: a) Modified oedometer cell b) Lathe used to trim soil samples.*

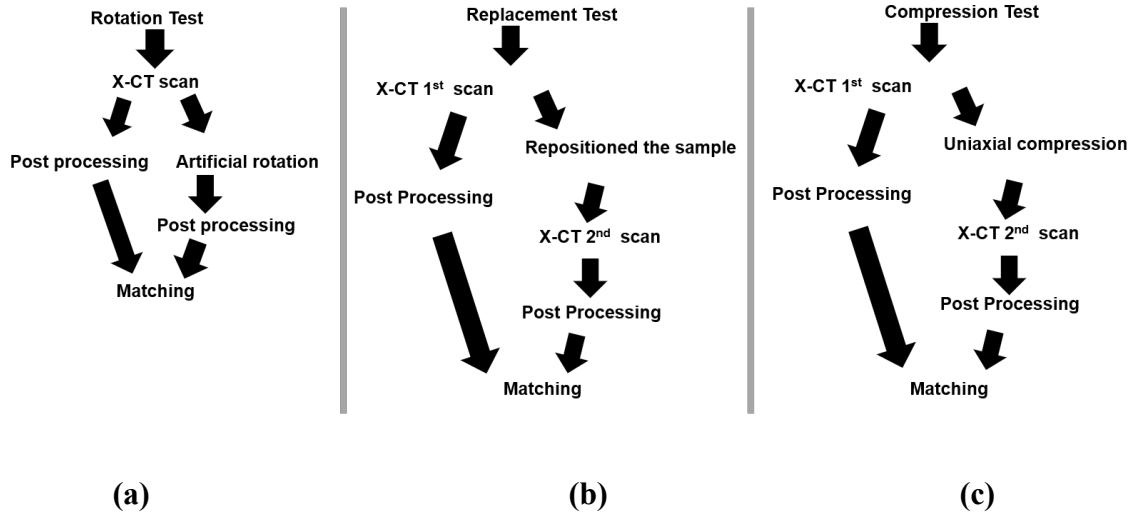
177

### 178 3 EXPERIMENTAL PROCEDURE

179 Three tests were performed using the lathe trimmed oedometer consolidated sample: a rotation  
180 test, a replacement test, and a compression test. For the rotation test, the sample was scanned  
181 and a section (2.9mm x 10mm) was digitally extracted from the scanned sample and artificially  
182 rotated by 5 degrees (see figure 3a and c). The original extracted section (without rotation) and  
183 the rotated image were then segmented and analysed. For the replacement test, the first scanned  
184 sample was re-scanned (i.e. the sample scanned, removed from the imaging stage, placed back  
185 on the imaging stage, and then rescanned), segmented, and the particle kinematics evaluated.  
186 Finally, the re-scanned sample was subjected to 8% uniaxial compression (using a plastic  
187 plunger loaded from bottom up) and the compressed sample scanned. By way of example,  
188 details of the third test are presented in figure 2 and table 2.

189 Images from the tests were processed as follows. First, we tried to match the mica particles in  
190 the compressed sample (compression test) using the matching code by Druckrey and Alshibli  
191 (2014) to evaluate the particle kinematics. The Druckrey and Alshibli (2014) approach was not  
192 originally designed for platy particles. We then adapted their approach by taking into  
193 consideration, the peculiar nature of platy particles as part of the image processing and particle  
194 matching workflow.

195 Secondly, we used the new PLATYMATCH approach. PLATYMATCH was initially applied  
196 to the rotation test to understand the effect of image remeshing due to rotation on particle  
197 attributes and for the evaluation of the best particle attribute for matching platy particles. It was  
198 then applied to the replacement test to evaluate the error associated with rescanning and image  
199 processing and finally applied to the compression test analysis (same test sample previously  
200 processed using the code by Druckrey and Alshibli, 2014).



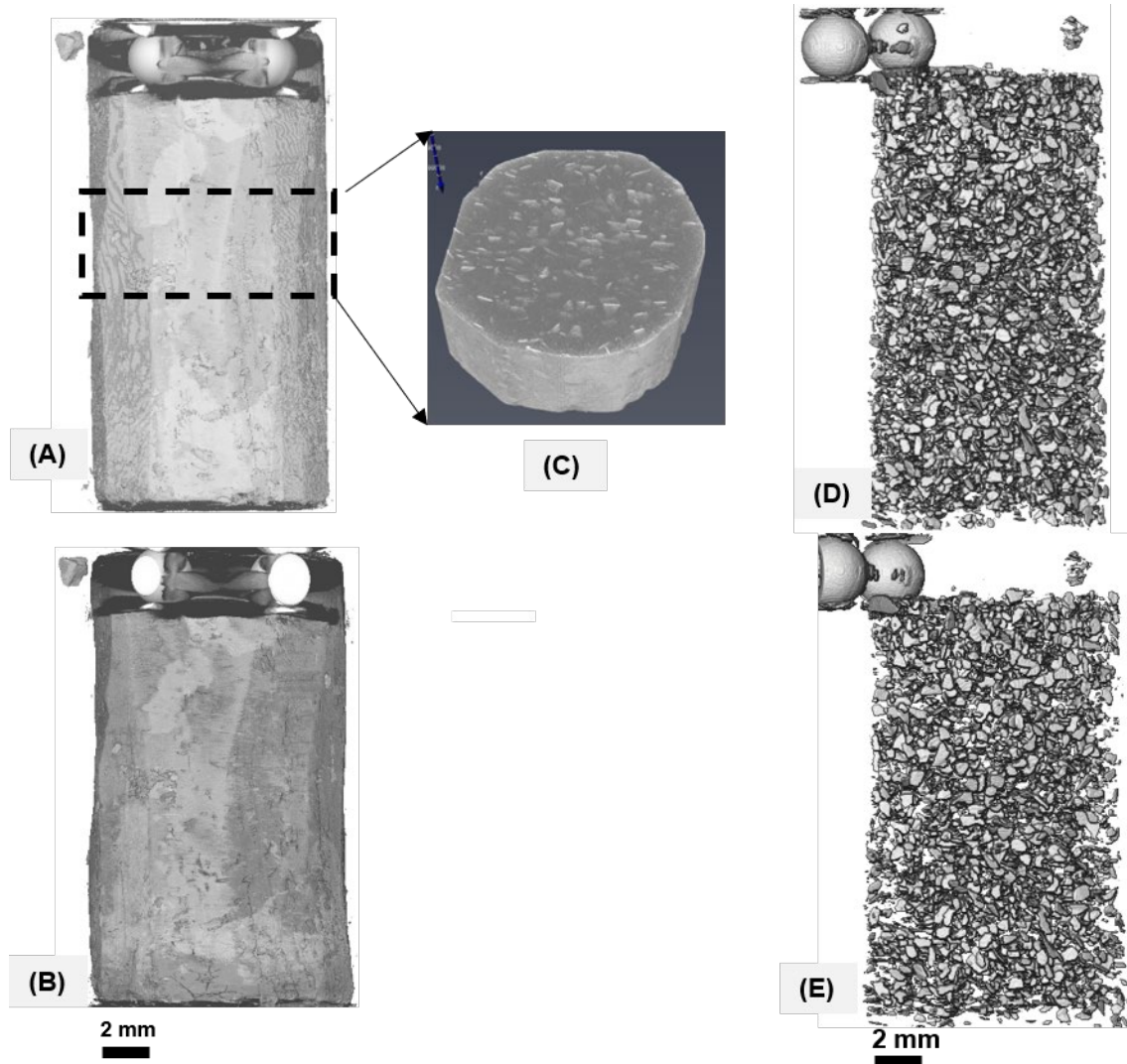
203 *Figure 2: The samples scanned and analysed: a) sub-section of a digitally extracted section of a main*  
 204 *scan, artificially rotated by 5 degrees; b) The main sample scanned, removed from the imaging stage,*  
 205 *replace and rescanned c) The rescanned sample subjected to 8% axial strain and scanned.*

206

207 *Table 2: Description of the samples for the three tests conducted.*

S/N	Image size	Sample size	Test
I	Sub-section of a digitally extracted section of a main scan, artificially rotated by 5 degrees	2.9mm height by 10 mm diameter	To understand of the effect of image remeshing due to rotation on particle attributes and evaluation of the best particle attribute for matching platy particles
II	Sample scanned, removed from the imaging stage, placed back on the imaging stage, and then rescanned	20mm height by 10 mm diameter	Evaluation of the error associated with rescanning and image processing.
III	Sample scanned, subjected to 8% axial strain and re-scanned	20mm height by 10 mm diameter	Validation of the matching code for a deformed sample

208



209

210 *Figure 3: 3D renderings of the tomography a) sample before compression b) Sample after*  
 211 *compression c) Artificially extracted sub section of the main sample d) segmented sample before*  
 212 *compression e) segmented sample after uniaxial compression.*

### 213 **3.1 Image Acquisition and processing**

214 The scans were acquired in-situ in the XTH320 NICON X-ray scanner at the University of  
 215 Strathclyde, which allows for 360-degree rotation of the sample. The voxel size of the 3D  
 216 tomographic image is  $10\ \mu\text{m} \times 10\ \mu\text{m} \times 10\ \mu\text{m}$ . X-ray energy of 160 kV and power 9.8 W and  
 217 exposure time of 1 second were used to image the samples. Each scan was reconstructed using  
 218 X-TEC commercial software and then processed using ImageJ software (<https://imagej.net>)  
 219 and Avizo-9 software (<https://www.fei.com/software/amira-avizo/>). To allow for later

220 registration, a metallic spherical ball (500  $\mu\text{m}$ ) was placed on the bottom side of the sample  
221 during scanning and used as a sample reference marker. In the compression test, the sample  
222 was imaged with the compressed end down and the stationary end up.

### 223 **3.2 Thresholding and Image classification**

224 The scans were first filtered using a Non-local means filter (Kumar 2013) because it preserved  
225 the mica particle edges, smoothed out the kaolin matrix to one constituent and enhanced the  
226 contrasts between the mica and kaolin. Following a conventional image processing approach,  
227 the image components were classified using absolute thresholding of the greyscale histogram  
228 after greyscale normalisation. See figure 20 in the Appendix for the grey scale histogram of the  
229 imaged sample. Each mica particle was then labelled using the interactive thresholding and  
230 label analysis tools in Avizo. The kaolin particles and mica particles have densities that are  
231 very close ( $\sim 2.7$  and  $2.8$  respectively), there is no clearly defined bimodal distribution in the  
232 greyscale histogram.

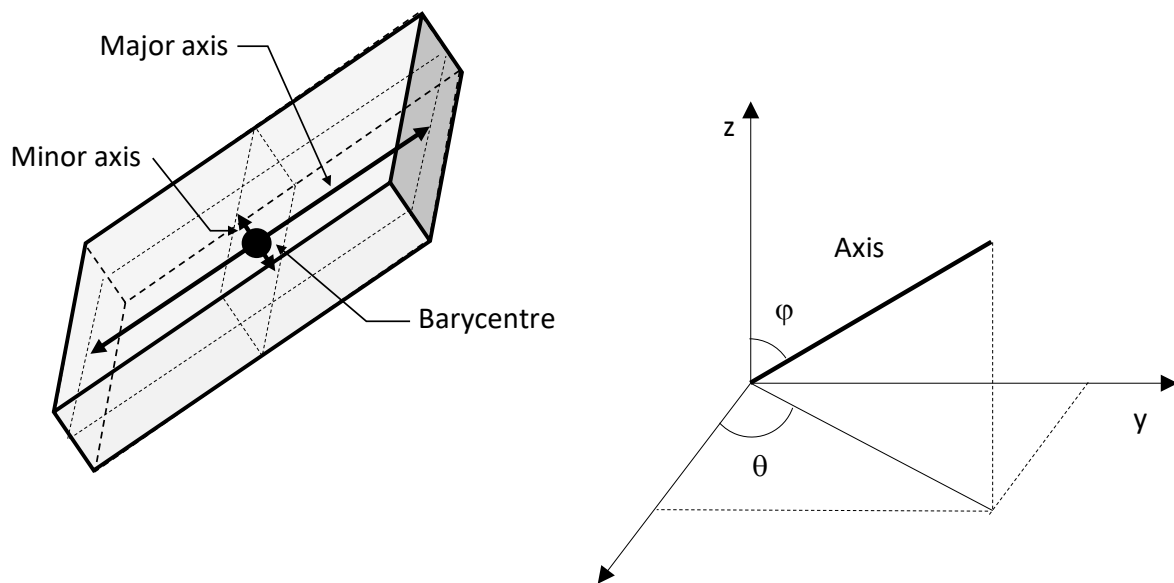
### 233 **3.3 Particle Property Measurement**

234 Particle properties required for implementing the matching algorithm by Druckrey and Alshibli  
235 (2014) were extracted. These properties included: position (x, y and z coordinates of the  
236 barycentre respectively), orientation (angles  $\varphi$  and  $\theta$  for the minor and major axes of the  
237 particle, see figure 4) and specific attributes: area, volume, Feret length and width (the distance  
238 between two parallel tangents of the particle on the maximum and minimum extent direction  
239 respectively). The attributes are those considered for particle matching, while the position and  
240 orientation data are used for particle kinematics (translation and rotation) and particle search  
241 regions. Additional geometry attributes derivable using Avizo were also extracted, they include  
242 particle perimeter (sum of particle edge length), major, intermediate, and minor axis lengths  
243 (these are derived as ExtentMax1, ExtentMax2 and ExtentMax3 in Avizo and correspond to

244 particle extents calculated in the direction of the smallest, intermediate and largest eigenvectors  
245 of the moment of inertia covariance matrix respectively).

246 The major [minor] axis is defined as the extent of the data in the direction of the smallest  
247 [largest] eigenvector of the covariance matrix (of the moments of inertia). It indicates the extent  
248 of the bounding box of the shape oriented along the corresponding eigenvector, with respect to  
249 the barycentre. The axis orientation in the x-y plane,  $\theta$ , ranges between  $-180^\circ$  and  $+180^\circ$ . The  
250  $\varphi$  angle formed by the particle axis with the z-axis (as shown in figure 4) ranges between 0 and  
251  $90^\circ$ .

252



253

254 *Figure 4: Orientation  $\varphi$  and  $\theta$  of particle major and minor axes*

#### 255 **4 IMPLEMENTATION OF MATCHING ALGORITHM BY DRUCKREY AND** 256 **ALSHIBLI (2014)**

257 The algorithm proceeds by first isolating a sub-section around each of the particle centroids in  
258 the first image (a cube centred on the particle centroid). The particle under consideration (in

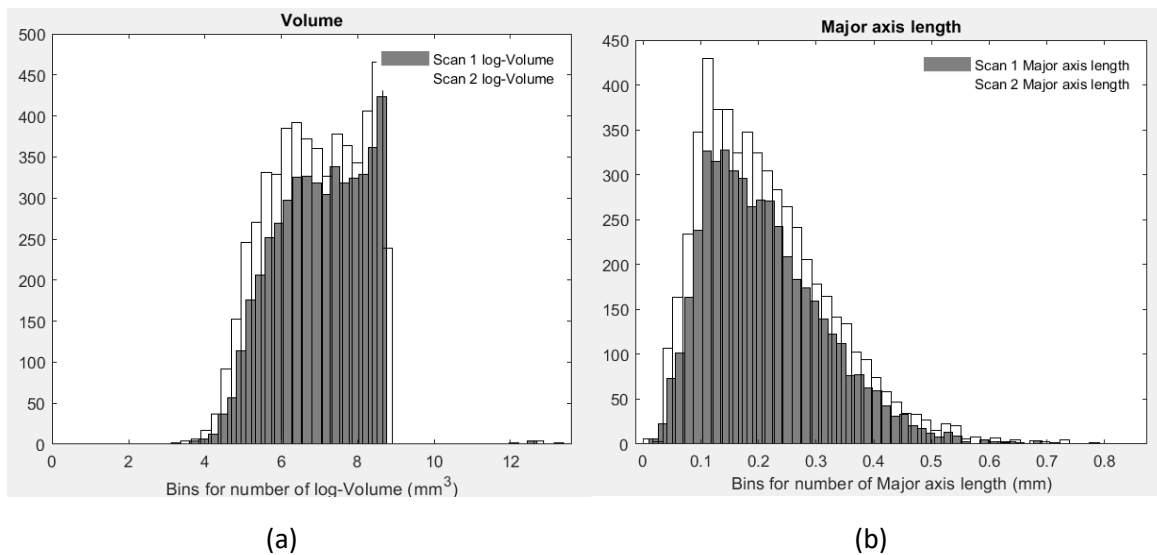
259 scan 1) is then searched for within the defined cubic sub-section in the second scan using a first  
260 particle morphology attribute (within a percentage error tolerance). A particle is not analysed  
261 if no particles were found in the following image within the defined sub-section. The sub-  
262 volume was then searched for particles within 5% the volume of the particle in the first image,  
263 and these particles are searched for particles within 5% surface area, followed by 5% length  
264 and finally 5% width of the particle in the first image. If more than one particle in the second  
265 image matches the search criteria for all attributes examined in series, the particle with the  
266 lowest error in the first attribute is matched. Thereafter the particle kinematics (displacement  
267 and rotation) are computed. The parameters used by this matching algorithm include: the size  
268 of the cubic search box centred on the particle centroid (chosen as a factor of the maximum  
269 imposed displacement. For example, 1.1 times the maximum macroscopic displacement  
270 observed, equal to  $1.6 \times 1.1 \text{ mm} = 1.76 \text{ mm}$  in the test discussed in the paper, as a guide), the  
271 matching attributes (volume, surface area, Feret length and width) and the matching attribute  
272 tolerance (5% according to Druckrey and Alshibli, 2014).

273

#### 274 **4.1 Initial Results for the compression test**

275 The matching was performed using the algorithm by Druckrey and Alshibli (2014) and resulted  
276 in only four particle matches despite increasing the percentage of acceptable attribute error to  
277 50%. To understand the problem, we first evaluated the effectiveness of the particle  
278 segmentation by conventional thresholding. Since the pre- and post-scans contain the same  
279 particles (if the particles do not significantly bend), we expect the statistical distributions of the  
280 various attributes to be the same for both scans. Figure 5 shows a comparison of the particle  
281 attribute distributions for particle volume and major axis length, with the distribution of scan 2  
282 (compressed sample) superimposed on scan 1 (sample before compression). A comparison of  
283 particle attributes between the initial and final scans shows a different number of particles.

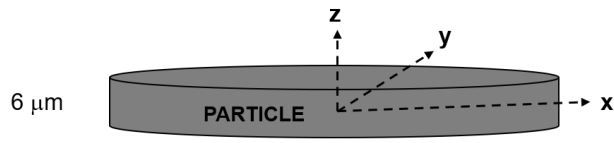
284 Nowhere near as many particles are identified, presumably because they are poorly segmented.  
285 These observations indicate that the scans are poorly classified using a conventional  
286 thresholding approach.



289 *Figure 5: Conventional thresholding segmentation result particle attribute histogram distribution for*  
290 *scan 1 and scan 2 a) Volume, b) Major axis length.*

291 Platy particles have a large specific surface area (ratio of external surface area to volume) and  
292 are highly non-spherical. Their small size and high specific surface area imply that, they  
293 contain far fewer voxels in comparison to round sand particles represented by the same voxel  
294 size and, hence, are liable to incur a larger particle segmentation error. For example, the tiny  
295 C-axis associated with the platy shape may give rise to artificial splitting of particles upon  
296 rotation. This is demonstrated in figures 6 a, b and c; if the threshold for considering a voxel  
297 as belonging to a particle is 50% then upon rotation of the particle (represented by dark grey  
298 voxels) the particle will artificially split. Figures 6d and 6e show two images, before rotation  
299 and after rotation, of voxels from the same particle, selected from the scan in Figure 3. The  
300 circle highlights where the particle has split into three after rotation (shown by the change in  
301 voxel colour from blue to yellow/green, as each segmented particle is plotted in a distinct  
302 colour).

303

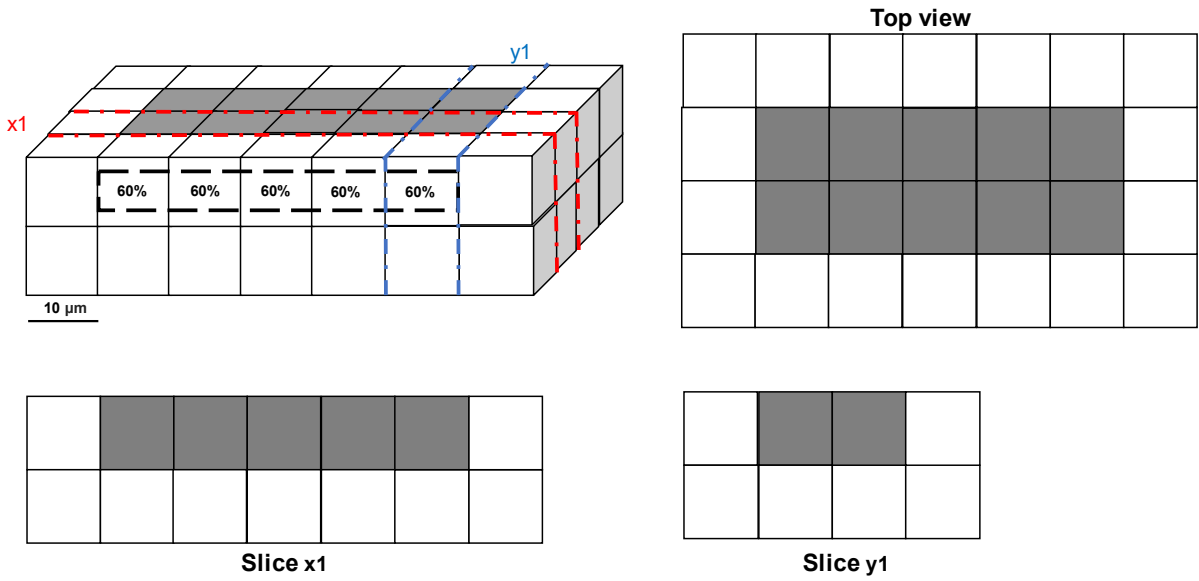


304

305

(a)

306

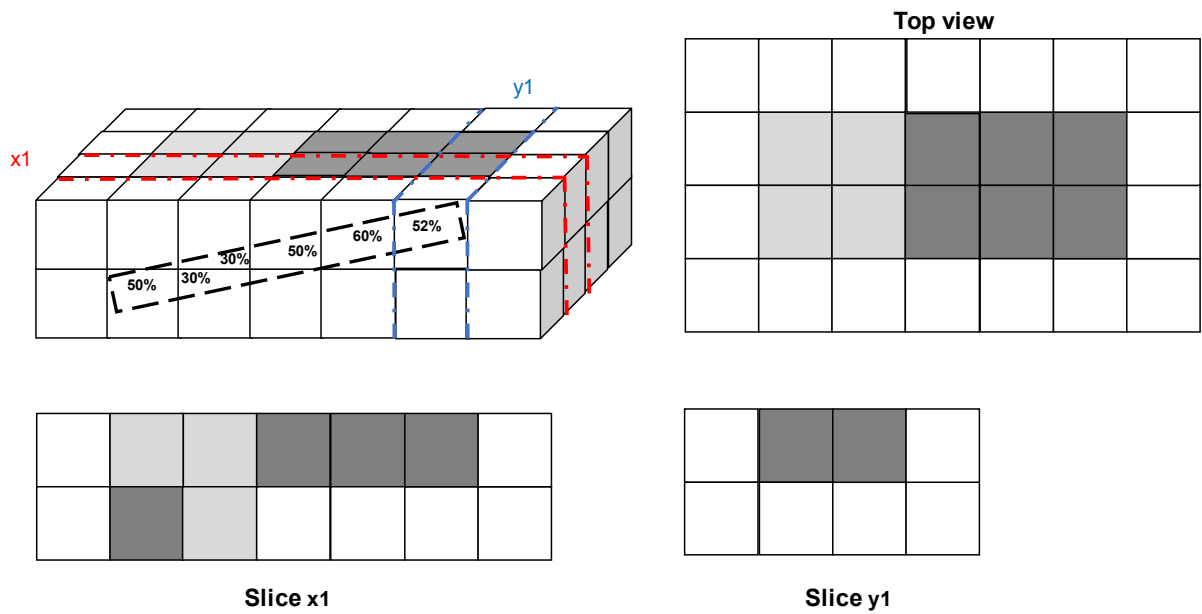


307

308

(b)

309



310

311

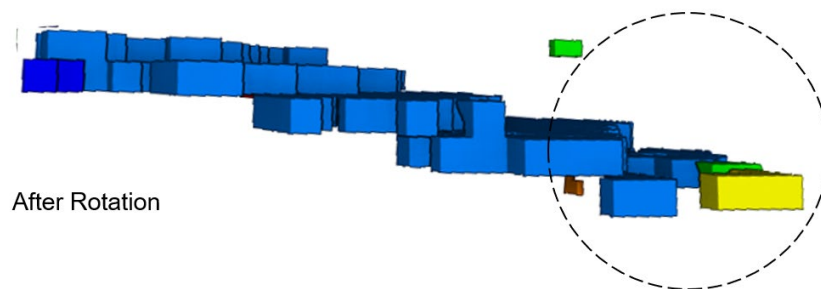
(c)



312

313

(d)



314

315

(e)

316 *Figure 6 (a) Platy particle (b) horizontal platy particle represented as voxels with the top view, slice-*  
317 *x1 and slice-y1 (c) same platy particle is slightly rotated and becomes artificially split into 2 because*  
318 *the 2<sup>nd</sup> voxel is below the 50% threshold for considering voxels as part of the particle, with the top*  
319 *view, slice x1 and slice y1 (d) intact particle before rotation (e) particle split after rotation (see*  
320 *the circular section with broken lines).*

321

322 As shown in Table 1, while the average number of voxels representing particle length of  
323 previous studies is at least 27 voxels, for a mica silt, it can be as small as 4 voxels. This is even  
324 worse for the platy mica silt particle C-axis, which may be as low as just 1 or 2 voxels. By  
325 comparison, in round sand particles there is only a slight reduction in the number of voxels  
326 representing the minor axis dimension compared to the major axis dimension. The limited  
327 achievable resolution and the small size of the platy particle C-axis dimension result in a large

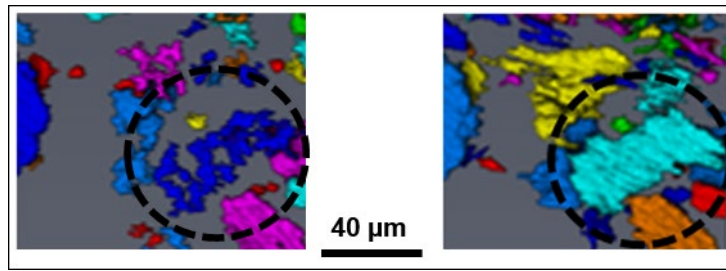
328 margin of error in the image segmentation. For a given particle, slight segmentation errors may  
329 result in a large difference in particles attributes between an initial scan and subsequent scans  
330 thus giving rise to erroneous match. There is therefore the need for a better segmentation  
331 approach for the platy particles.

332

333 To improve particle segmentation, we used the Trainable WEKA machine learning  
334 segmentation (TWS) tool (Arganda-Carreras et al. 2017), a machine learning segmentation tool  
335 that has been applied successfully by researchers to discriminate other thin objects such as  
336 fibres (Madra et al 2014 and Karamov et al 2019). TWS is open source code that combines the  
337 advantages of human knowledge, intensity and the spatial relationship of voxels with machine  
338 learning for an improved accuracy of the labelled region. It leverages a limited number of  
339 manual annotations to train a classifier and segment the remaining data automatically  
340 (Arganda-Carreras et al. 2017). To give an objective classification of each scan, the TWS  
341 model was trained using a combination of the sub- sections of the two scans to be compared.  
342 The process proceeded as follows: First, the images to be classified were filtered (in this case,  
343 using a non-local means filter). Then, a section of each filtered image was cut and imported  
344 into TWS and combined. The pixels were classified as either being kaolin, mica or the  
345 background – see figure 18, Appendix 1. This set of labelled input pixels were then used as a  
346 training set for the classifier and the trained model was used to classify the whole sample image.  
347 Figure 19 (Appendix 1) shows the distribution of the mica particles intermediate length after  
348 TWS was used, which was consistent with the image resolution.

349 Figure 7 below shows the difference between a mica particle segmented using the conventional  
350 segmentation technique (thresholding) and using the TWS. It is clear that due to the thin nature  
351 of the platy particles, the conventional technique has a tendency to split the particles into  
352 multiple smaller plates whereas this problem was minimised using the TWS technique.

353

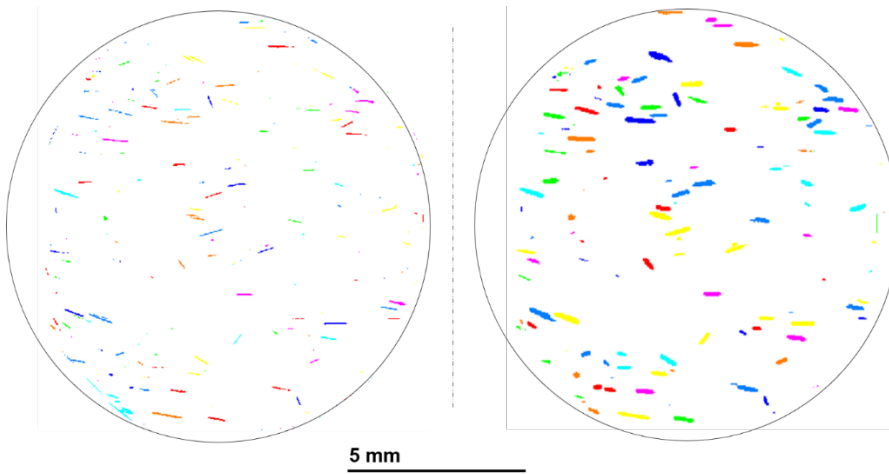


354

355

(a)

(b)



356

357

358

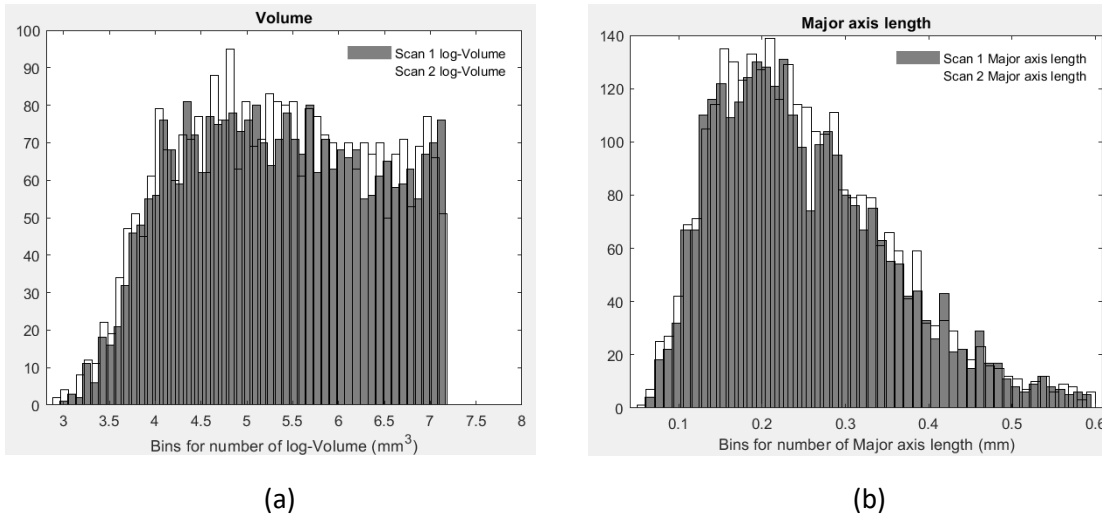
(c)

(d)

359 *Figure 7: Image segmentation performed on sub-sample image volume using (a) absolute*  
360 *thresholding (b) TWS (c) 2D images of a sample classified using absolute thresholding (d) 2D images*  
361 *of a sample classified using TWS,*

362

363 Figure 8 shows the pre- and post-deformation scan distributions for the same particle attributes  
364 as in Figure 5 (Volume and Major axis length) but using the TWS technique. The results are  
365 considerably improved, with very similar total particle numbers and attribute distributions  
366 between the two scans.



367

368

369

370

371

372

373

374

375

376

377

378

379

380

381

382

383

384

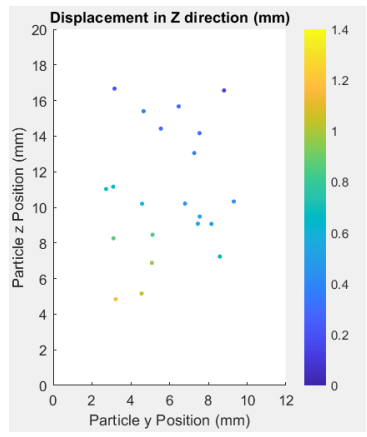
385

*Figure 8: TWS segmentation result for Particle attribute histogram distribution for scan 1 and scan 2  
a) Volume, b) Major axis length.*

Using the TWS particle segmentation method, particles of the initial sample scan and the loaded sample scan were then re-matched using the algorithm of Druckrey and Alshibli (2014). Again, the parameters used by this matching algorithm include: the search box centred on the particle centroid (different search box sizes were run to get the best search box size), the matching particle attributes volume, surface area, feret length, and feret width. Various scenarios considering different search box sizes and particle attribute error tolerance were run to achieve the best possible appropriately matched particles. Matching attribute tolerance errors of 2%, 5%, 7% and 10% respectively were considered.

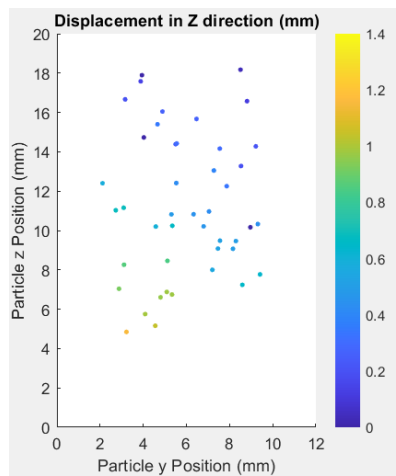
With a 2% attribute error tolerance, no particle was matched. Figures 9 a, b and c show plots of particle y-z-position against particle z-displacement, for attribute error tolerances of 5%, 7% and 10% respectively. It can be observed that with increasing error tolerance, more particles are matched, but as expected this also results in increasing numbers of wrongly matched particles. An increase in attribute error tolerance to 20% resulted in numerous erroneous matches. Although the match gives an overview of the sense of movement of the particles

386 (which is from bottom up, as the sample was scanned with the stationary end at the top), the  
387 number of particles matched in the test with 10% error tolerance was 95, which represents 4%  
388 of the total number of particles segmented.



389

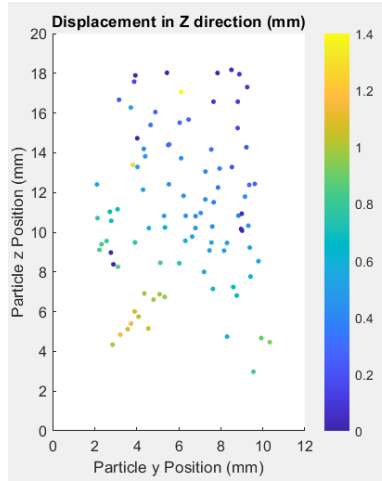
(a)



391

(b)

392



393

394

(c)

395 *Figure 9: Result of particle matching using the algorithm by Druckrey and Alshibli (2014) a) Particle*  
 396 *z-axis displacement with a 5% error tolerance, b) Particle z-axis displacement with a 7% error*  
 397 *tolerance c) Particle z-axis displacement with a 10% error tolerance.*

398 Figure 9 highlights the need to determine and evaluate unique platy particle attributes that can  
 399 adequately match a larger number of particles with a low error tolerance. To investigate which  
 400 particle attributes might be the most effective, the statistics of each attribute were compared  
 401 between scans. Since both scans contain the same particles, the standard deviations of each  
 402 particle attribute should be the same. Table 3 shows the normalised difference of the standard  
 403 deviations (as a percentage) for each particle attribute. The Minor axis length gives the largest  
 404 normalised difference, followed by Volume, Feret Width, Area, Intermediate axis length,  
 405 Perimeter, Feret Length and the Major axis length. Although Feret length gives a low  
 406 normalised difference, it is not a robust attribute for platy particles, since under some loading  
 407 conditions platy particles may flex, hence this parameter was not examined further.

408

$$409 \left( \frac{Sd_1 - Sd_2}{Sd_2} \right) \times 100 \quad [1]$$

410 Where  $Sd_1$  is the scan 1 standard deviation of the attribute under consideration and  $Sd_2$  is its  
 411 scan 2 standard deviation.

412

413 *Table 3: Percentage normalised difference of standard deviation of particle attributes before and*  
414 *after sample compression.*

415

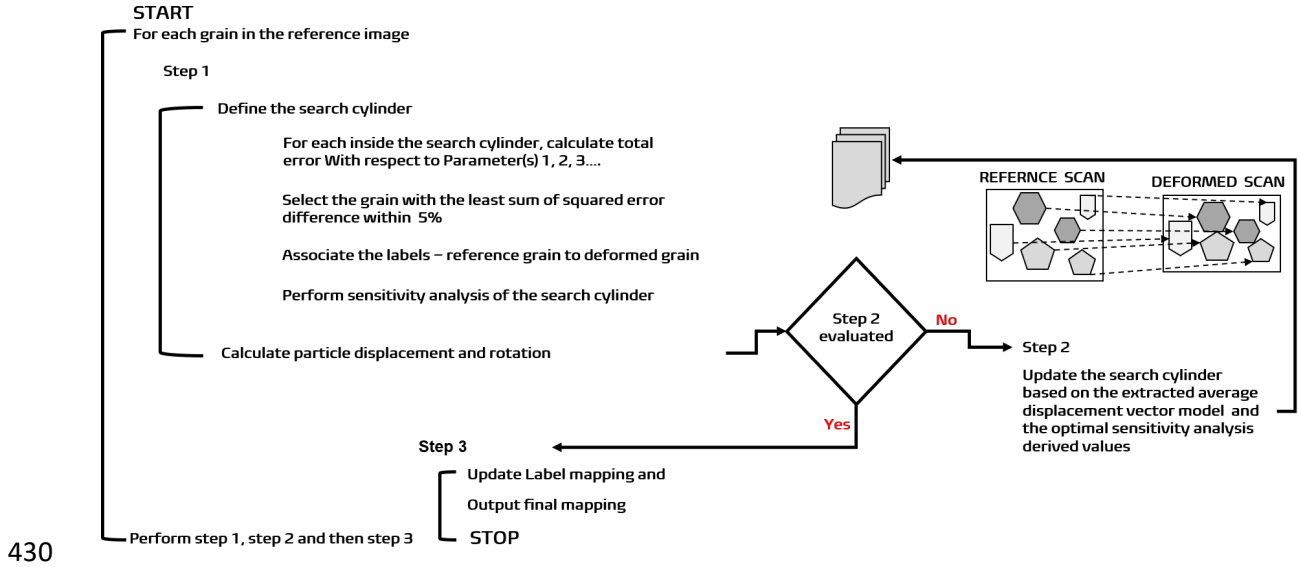
<b>ATTRIBUTE</b>	<b>% Normalised difference</b>
Minor axis Length	8.7719
Volume	6.7568
Feret Width	5.8236
Area	3.4331
Intermediate axis Length	1.7595
Perimeter	1.1205
Feret Length	0.1954
Major axis Length	0.0963

416

## 417 **5 PLATYMATCH FRAMEWORK**

418 The approach of Druckrey and Alshibli (2014) was adapted to match plat-shaped particles. To  
419 minimise the issues associated with any remaining segmentation errors, the particle match was  
420 optimised based on the calculation of a combined ‘attribute error statistics’, as opposed to the  
421 approach based on the assessment of each attribute error in a sequential fashion, which can lead  
422 to potential particle matches to be overlooked (particles that do not match the first attribute of  
423 the sequence are discarded and not considered anymore when the second attribute is examined  
424 and so on). Second, the process was optimised by determining the combination of particle  
425 attributes that best discriminates individual particles and hence maximises the number of  
426 particles matches that can be reliably obtained.

427 Figure 10 shows the workflow for PLATYMATCH. The code implements a least square error  
428 optimization workflow in MATLAB to match particles from one scan to another with a given  
429 error tolerance. The workflow proceeds as follows.



431 *Figure 10: PLATYMATCH workflow*

432 First, we define  $x_{ik}$  as the value of the  $k^{\text{th}}$  attribute for particle number  $i$  in scan 1, where  $k=1, \dots, q$   
 433 and  $q$  is the total number of attributes. So for example, if we used volume, area and perimeter,  
 434  $q=3$  and  $x_{i1}$ ,  $x_{i2}$  and  $x_{i3}$  would be the values of volume, area and perimeter respectively for  
 435 particle  $i$  scan 1.

436

437 Particles are then matched as follows. For each particle  $i$  in scan 1, where  $i=1, \dots, n$  and  $n$  is the  
 438 total number of particles in scan 1, a search cylinder is defined in scan 2, the centre of which  
 439 is the coordinate of the barycentre of particle  $i$  in scan 1. If each cylinder in scan 2 contains  $m$   
 440 particles, then in order to find the best particle match for particle  $i$ , PLATYMATCH calculates  
 441 the sum of the normalised square differences in the particle attribute values,  $\Lambda_{ij}$ , for each  
 442 possible matching particle  $j = 1, \dots, m_i$  in the search cylinder in scan 2:

443

444 
$$\Lambda_{ij} = \sum_{k=1}^q \left[ \frac{\sqrt{(x_{ik}^2 - x_{jk}^2)}}{x_{ik}} \right] \quad [2]$$

445

446 Then, particle  $j_{match}$  is the matched particle if

447

$$448 \quad \Lambda_{ij_{match}} = \min_{j=1,\dots,m_i} \{\Lambda_{ij}\} \quad [3]$$

449 and  $\Lambda_{ij_{match}} <$  user defined error threshold. If  $\Lambda_{ij_{match}} >$  the error threshold then the  
450 particle match is discarded and no match for particle  $i$  is achieved.

451 Particle displacement is calculated as the Euclidian distance between particle initial and final  
452 position.

$$453 \quad Displacement = \sqrt{(X_1 - X_2)^2 + (Y_1 - Y_2)^2 + (Z_1 - Z_2)^2} \quad [4]$$

## 454 **6 PLATYMATCH IMPLEMENTATIONS**

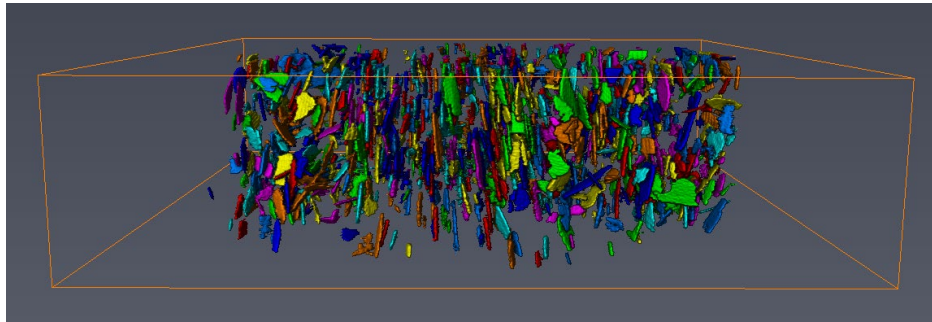
455 PLATYMATCH was evaluated using three tests. The first ‘Rotation’ test was conducted to  
456 understand which particle attribute produced the largest number of adequately matched  
457 particles, whilst maintaining a satisfactorily low error tolerance. The second ‘Replacement’ test  
458 was conducted to evaluate the effect of sample image processing on particle matches. Finally,  
459 the code was used to match the particles and analyse the particle kinematics of the Compression  
460 test presented earlier.

### 461 **6.1 Evaluation of particle matching attributes using the artificially rotated sample**

#### 462 **(Rotation Test) – Attribute Analysis.**

463 In this test, the sample was reconstructed, processed to identify the particles, and the particles  
464 attributes extracted for ‘scan 1’. The scan was then artificially rotated by 5 degrees along the  
465 y-z- plane (within Avizo), then re-processed and the new particle attributes obtained for ‘scan  
466 2’. Figure 11 shows the segmented sample before and after rotation.

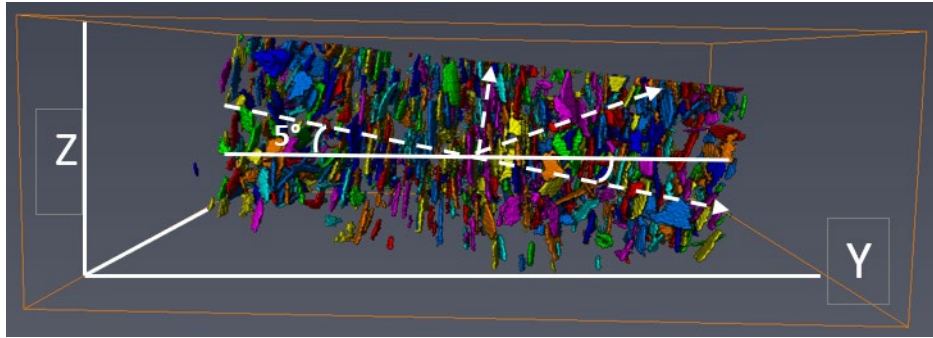
467 The uniqueness of the attributes with respect to the platy nature of mica particles were  
468 evaluated to determine which attribute or attributes may be more suited for matching the platy  
469 particles considering the platy nature of the particles and their relatively small *c*-axis compared  
470 to the resolution of the X-CT. The use of derived attributes (attributes resulting from  
471 mathematical combination of basic morphological attributes- primary attributes) instead of  
472 primary attributes may present some challenges due to larger error and uncertainty in their  
473 values. Hence it is proposed that using primary attributes that are not functions of the minor  
474 axis (*c*-axis) length and do not change significantly with sample deformation will be a more  
475 unique identifiers, enabling effective platy particle matching across scans.



476

477

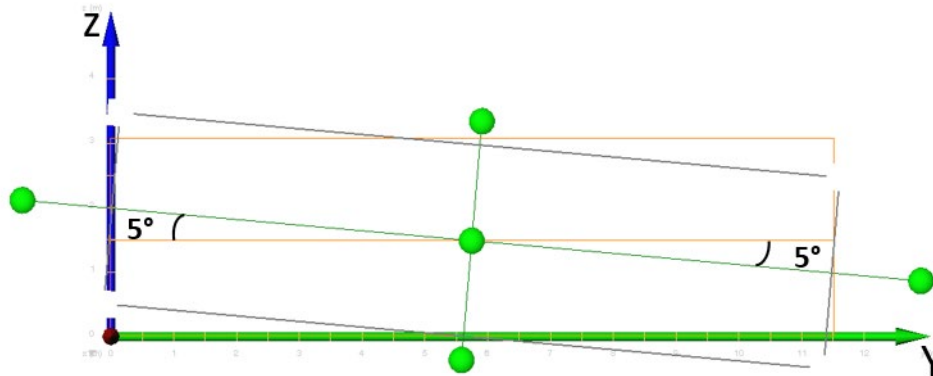
(a)



478

479

(b)



480

481

(c)

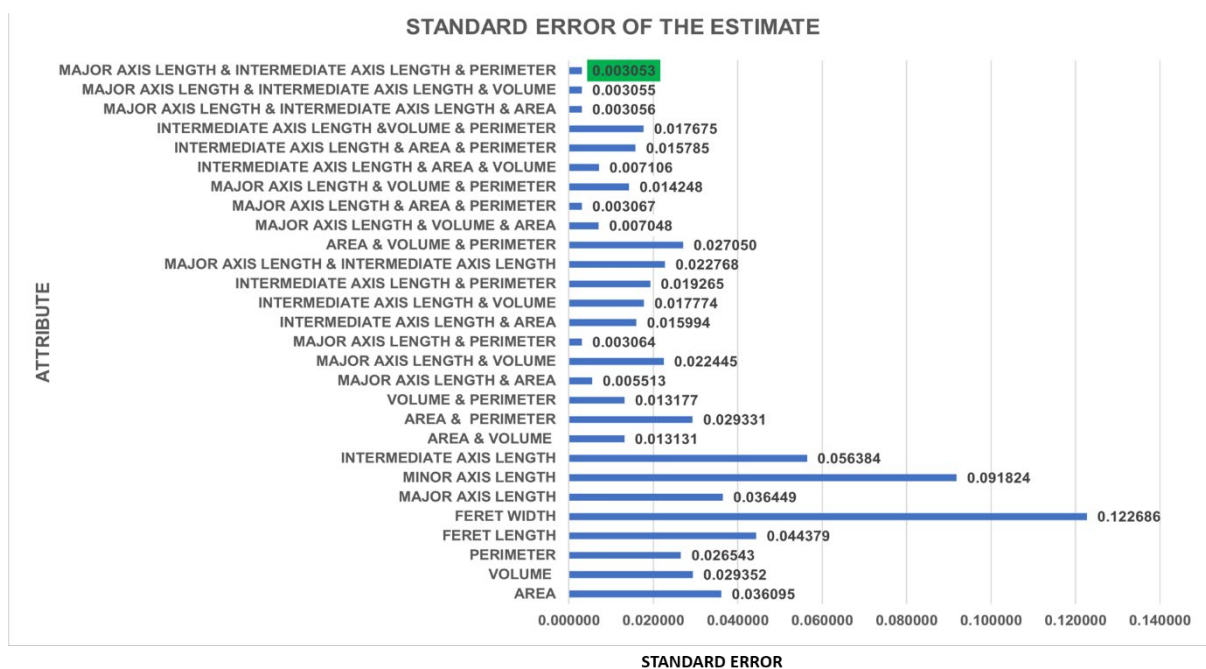
482 *Figure 11: a) sample after image processing and segmentation but before rotation b) sample after 5*  
 483 *degrees rotation along the y-z plane c) sample sense of rotation, the orange line indicates the initial*  
 484 *sample boundary and the grey line indicate the sample boundary after the 5 percent rotation.*

485 To understand the particle attribute or attribute combination that give the best match, each  
 486 attribute was used individually in turn to match the particles between the two scans. Particle  
 487 attributes used were volume, perimeter, area, major axis length, and intermediate axis length,  
 488 minor axis length, Feret length and Feret width. Attributes that appeared to give an accurate  
 489 match were then tested in combination to find the optimum combination of attributes for  
 490 accurately matching of platy particles.

491 Results are given in Figure 12 and are expressed as the standard error in the z-coordinate  
 492 displacement values, which are imposed by the 5° rotation and therefore known. No single

493 attribute gave a z-displacement error of less than 1% between scans. The least error was  
 494 achieved using an attribute combination of the Major axis length, the Intermediate axis length,  
 495 and the Perimeter.

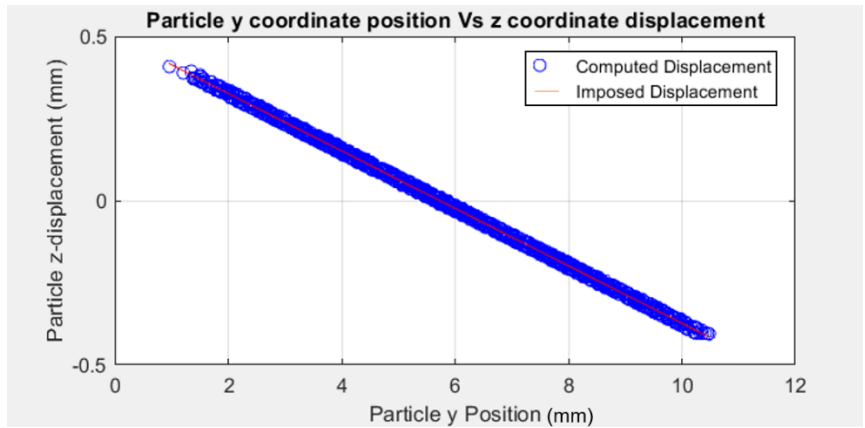
496 Detailed results from combining these three attributes are shown Figure 13a to c. Figure 13a  
 497 compares the imposed and computed z-displacements showing a satisfactory agreement.  
 498 Figure 13b clearly shows the rotational trajectory of each matched particle (the view is taken  
 499 along the axis of rotation). Figure 13c shows the statistical distribution of the z-displacement  
 500 error (difference between imposed and computed displacement) in terms of empirical  
 501 cumulative distribution. This is characterised by a mean of 0.3  $\mu\text{m}$  and a standard deviation  
 502  $\approx 3.0 \mu\text{m}$ . The figures also show the normal cumulative and frequency distributions associated  
 503 with these values of mean and standard deviation, which shows that the error is essentially  
 504 normally distributed. Errors are likely to be a result of small changes in the voxels used to  
 505 describe a particle between scans that result in slight changes to the particle segmentation. This  
 506 can cause the centre of inertia of a particle to be located in a slightly different position within  
 507 the particle between scans, thus resulting in a small displacement error.



508

509 *Figure 12: Standard error of Z-coordinate displacement using matched particles for all attribute and*  
510 *attribute combinations, with a combination of major axis length and perimeter giving the least*  
511 *standard error of the estimate*

512



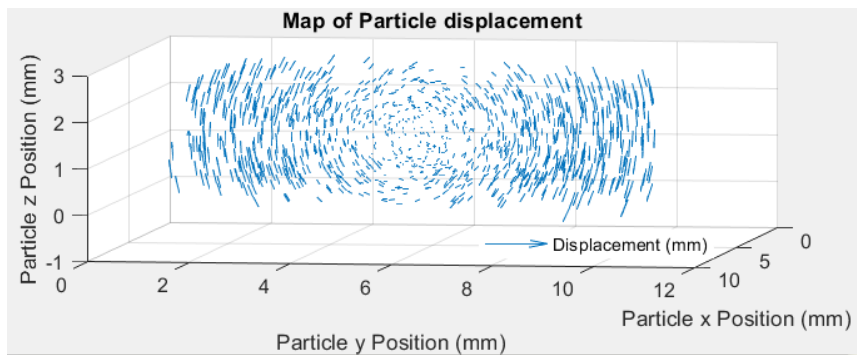
513

(a)

514

515

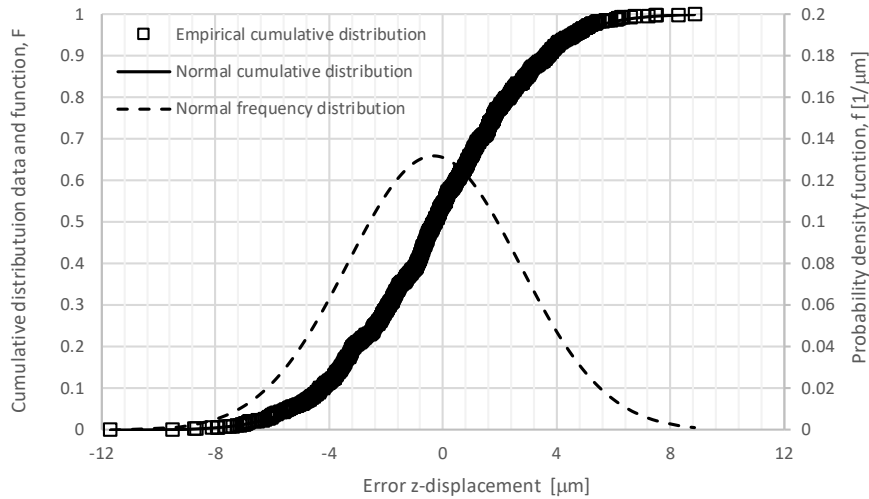
516



517

(b)

518



519

520

(c)

521 *Figure 13: Sample artificially rotated 5° in the y-z plane and unregistered matched to the original*

522 *sample (without rotation) using Major axis length, and Perimeter as PLATYMATCH search*

523 *attributes. a) particle y position against z- coordinate displacement; b) displacement vectors; c)*

524 *Cumulative and frequency distribution of the z-coordinate displacement (mean=0.3 μm and standard*

525 *deviation=3.0 μm)*

526

527 **6.2 Evaluation of particle matching accuracy, using a sample that was scanned,**

528 **removed, and replaced and re-scanned (Replacement Test).**

529 In the Replacement Test, particles have not been displaced (there is no rotation or translation

530 of the image so they should remain virtually in the same location between the two scans). The

531 differences between the two scans should only depend on the ability to align the two scans (i.e.,

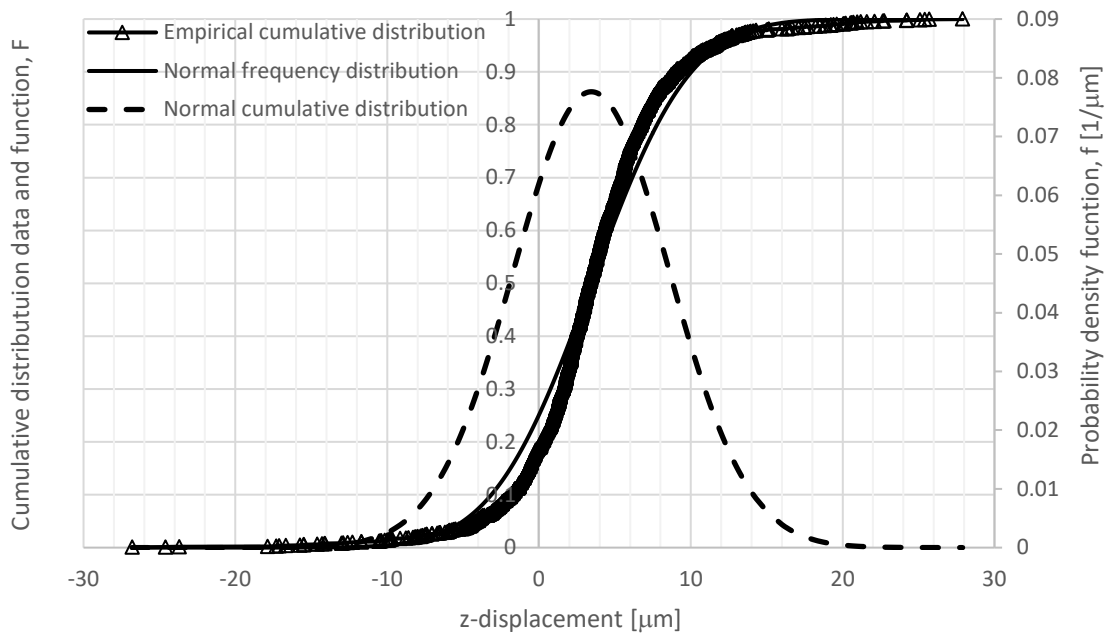
532 to accurately co-locate the ‘marker’ steel spheres that were inserted into the sample). The two

533 scans were processed, registered and then the particles matched using PLATYMATCH. The

534 matching was performed using Major axis length, and Perimeter as PLATYMATCH search

535 attributes and a 5% error tolerance.

536 Figure 14 shows the statistical distribution of the z-displacements in terms of empirical  
 537 cumulative distribution. This is characterised by a mean of 3.4  $\mu\text{m}$  and a standard deviation  
 538  $\approx 5.1 \mu\text{m}$ . The figures also show the normal cumulative and frequency distributions associated  
 539 with these values of mean and standard deviation, which shows that the error is essentially  
 540 normally distributed. The result is consistent with an expected displacement of zero; the scan  
 541 resolution was at 10 micrometres, hence a z-coordinate displacement cumulative and frequency  
 542 distribution with a mean of 3.4  $\mu\text{m}$  and standard deviation of 5.1  $\mu\text{m}$  is within the resolution of  
 543 the scan.



544

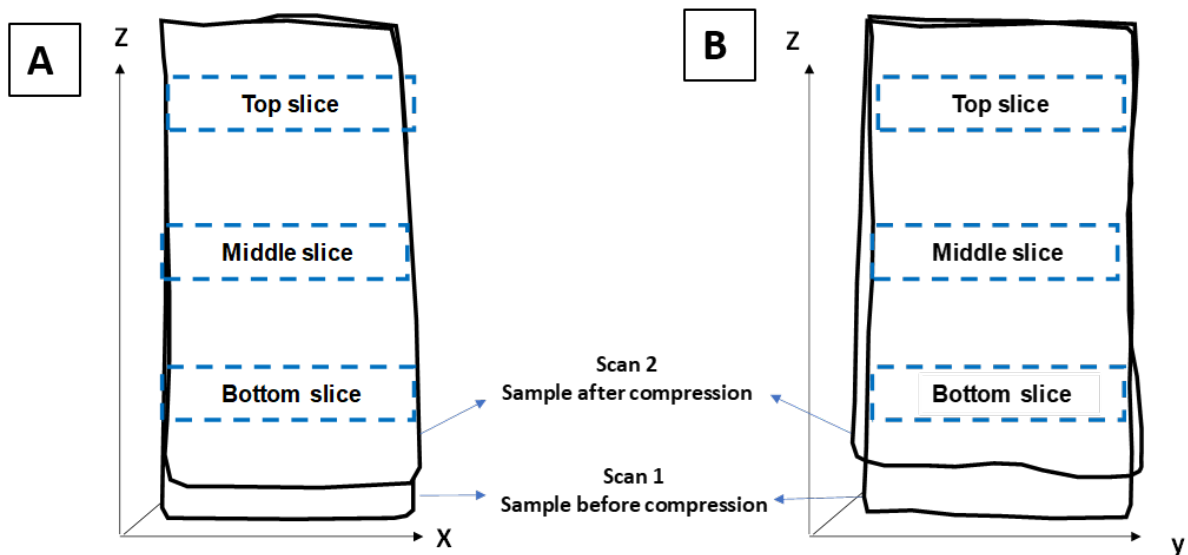
545 *Figure 14: Cumulative and frequency distribution of the z-coordinate displacement (mean=3.4  $\mu\text{m}$*   
 546 *and standard deviation=5.1  $\mu\text{m}$ ) .*

547

### 548 **6.3 Particle tracking after unconfined uniaxial compression (Compression Test)**

549 To validate the matching code on a genuine tracking problem, the sample subjected to 8%  
 550 uniaxial strain, was analysed for particle kinematics. The sample was scanned with the fixed

551 end at the top and the compressed end at the bottom and thus was expected to show higher  
 552 axial deformation at the bottom compared to the top where motion is restricted. The axial  
 553 deformation recorded at the bottom by the XCT scan is also expected to be less than the  
 554 imposed deformation, since the sample experienced some rebound when it was unloaded and  
 555 removed from the loading frame, prior to the second scan. Since the sample was laterally  
 556 confined by a rubber membrane, radial deformation was expected to occur with higher values  
 557 at the bottom (which was being compressed) compared to the top (which is fixed). The sample  
 558 profile in the x-z and y-z planes before and after compression are shown in Figure 15 and  
 559 confirms that the sample was deforming in both axial and radial directions.



560

561 *Figure 15: Kinematic analysis of clay sample subjected to 8% axial compression a) particle*  
 562 *displacement map along the z-y plane b) Particle displacement vector map in the x-z plane.*

563

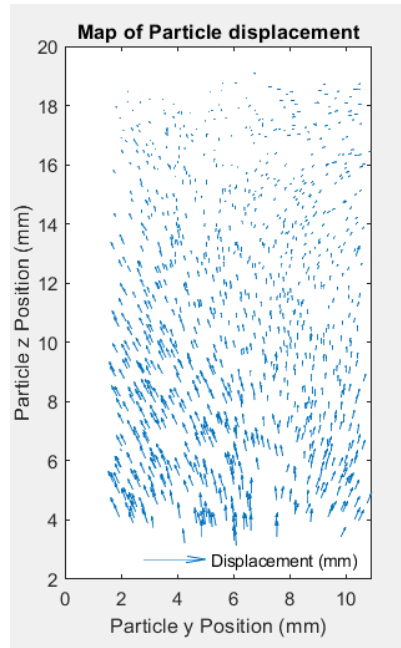
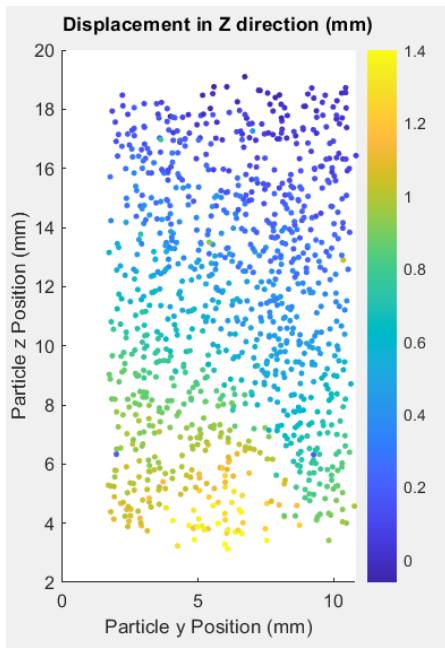
564 Mica particles before and after uniaxial compression were matched to evaluate particle  
 565 kinematics. As in the previous analysis, Major axis length, Intermediate axis length and  
 566 Perimeter were used to match the particles with PLATYMATCH. The number of particles  
 567 matched in the test was 1035, which represents 40% of the total number of particles segmented.

568 The slightly low percentage of particles matched may be due to the relatively large  
569 displacement step applied in the uniaxial compression test (8% strain).

570 Figures 16 show results of the particle displacements for the sample subjected to an 8% axial  
571 strain, with figure 16a showing the displacement map along the z-y plane and figure 16b  
572 showing the particle displacement vectors in the x-z plane. As expected, the particle trajectory  
573 distances reduce from a maximum of 1.4 mm at the bottom of the image to zero at the top.

574 Interestingly, the result in Figure 16b show that the sample does not deform in a homogeneous  
575 manner. The displacement vectors are not all parallel to the z-axis, i.e., the displacement vectors  
576 have a horizontal component. This is consistent with the profiles shown in Fig. 15. To explore  
577 the displacements in the x-y plane, three slices were considered as shown in Fig. 15. The  
578 horizontal component of the displacement of the mica particles contained within these three  
579 slices are shown in Fig. 17. The sample is subjected to a slight torsional deformation. When  
580 this torsional deformation is discounted, the remaining displacement is radial, which is  
581 consistent with the sample profiles shown in Fig. 15.

582 In the interpretation of the tracking results presented here for uniaxial compression, particle  
583 kinematics were only analysed in terms of displacements of their barycentre. However, because  
584 particles are platy, analysis of particle orientation may give interesting insights into shear  
585 strains, as compared to spherical particles. This may allow a greater understanding of concepts  
586 such as initiation and propagation of strain localisation and dilation.

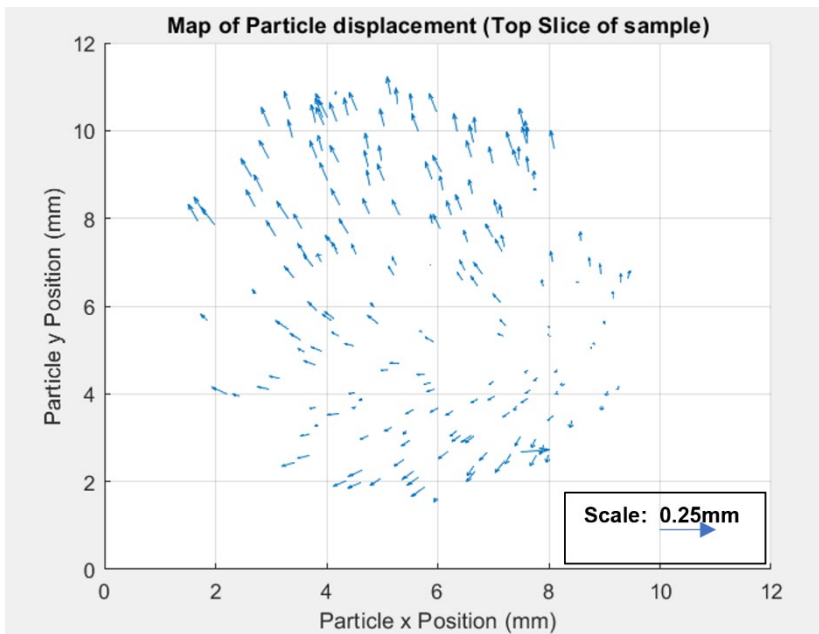


587 a)

b)

588 Figure 16: Kinematic analysis of clay sample subjected to 8% axial compression a) particle  
 589 displacement map along the z-y plane b) Particle displacement vector map in the x-z plane.

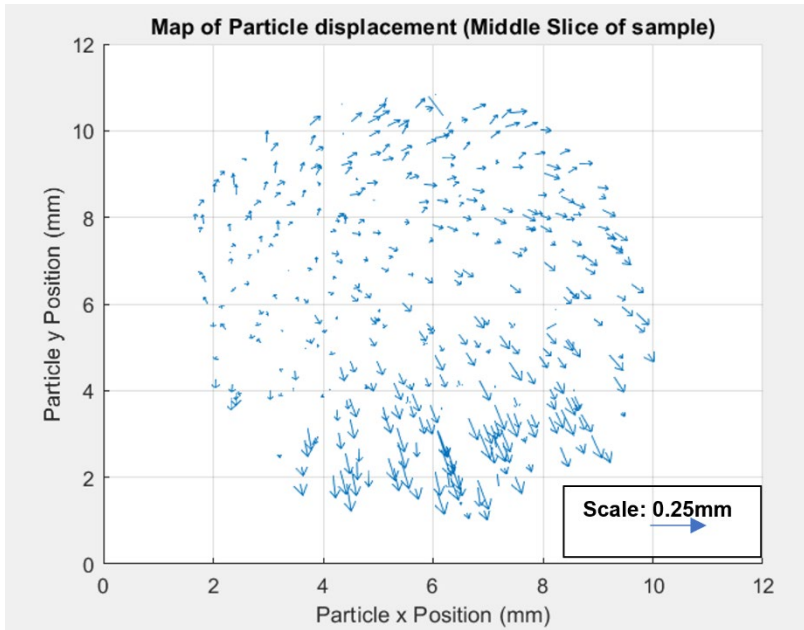
590



591

592

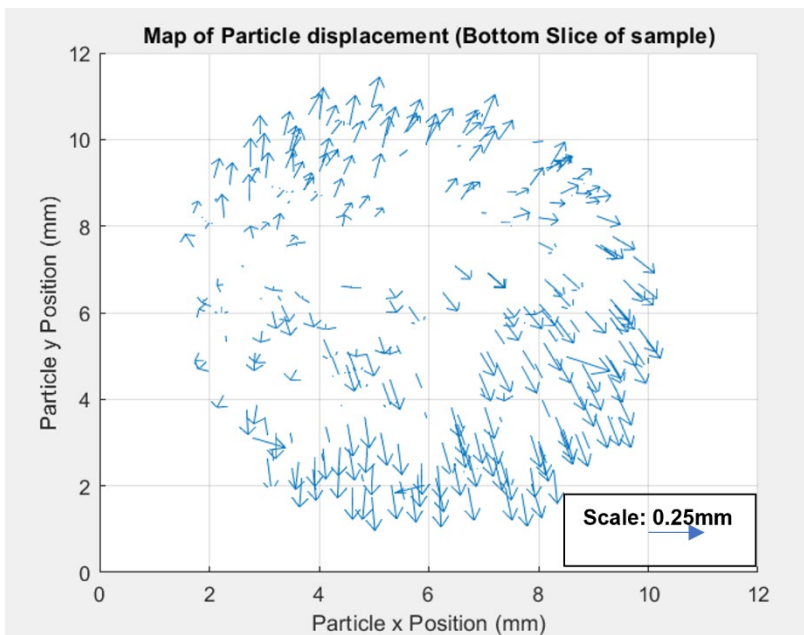
(a)



593

594

(b)



595

596

(c)

597 Figure 17: Horizontal slice of displacement vectors of compressed sample at the a) top section b)  
 598 middle section and c) bottom section. (Note that the scale of the displacement vector – arrows, is  
 599 magnified by a factor of 4).

## 600 7 CONCLUSIONS

601 This study evaluates, for the first time, kinematic analysis of platy soil particles through  
602 individual particle matching. Particles were first matched using an existing algorithm  
603 successfully developed for matching sand round particles. Some challenges were observed due  
604 to the small size and platy nature of mica. Attributes such as: Feret width, Feret length, minor  
605 axis length, which may be unique for round sand particles were observed to be significantly  
606 less unique to the platy particles studied. This was due to their tiny c-axis and smaller overall  
607 size, which resulted in a poorer image resolution and segmentation errors.

608 We adapted the matching code by Druckrey and Alshibli 2014 (which was originally designed  
609 for matching sand particles) by incorporating attributes and workflows that are best suited for  
610 platy particles to form a matching algorithm – PLATYMATCH. We evaluated platy mica silt  
611 particle attributes to identify unique attributes successful at matching platy particles.  
612 PLATYMATCH considers a minimised combined normalised error of parameters of particles  
613 within a defined search volume space. Parameters of the algorithm are: location and size of the  
614 search volume space, the selected combination of particle geometric attributes and the error  
615 tolerance.

616 The code was tested using a clay sample with mica particle markers subjected to uniaxial  
617 compression. The following conclusions were drawn:

618 i) Correctly implemented, a voxel training machine learning algorithm gave optimal  
619 segmentation results compared to threshold segmentation and hence enhanced particle  
620 matching. For objective comparison using the machine learning segmentation, it was important  
621 to train the machine learning algorithm using both ‘before’ and ‘after’ scans.

622 ii) A combination of particle attributes: major and intermediate axis length and perimeter gave  
623 the best particle match, when compared to other particle attributes. Due to the larger errors in

624 segmentation found on platy particles, the particle attributes should be compared in parallel,  
625 rather than sequentially, which avoided filtering out good particle matches based on a single  
626 attribute and resulted in a greater number of correctly matched particles.

627 iii) PLATYMATCH can effectively match platy particles when consecutive scans are  
628 adequately registered and particles within scans are adequately segmented.

629

630

631

632

633

634

635

636

637

638

639

640

641

642

643

644

645 **ACKNOWLEDGEMENTS**

646 The publication of this work was made possible through support from the University of  
647 Strathclyde Research Studentship. We also acknowledge the support of Mr Derek McNee in  
648 assembling the modified oedometer cell and soil Lathe designed in this study.

649 **DATA AVAILABILITY STATEMENT**

650 Some or all data, models, or code that support the findings of this study are available from the  
651 corresponding author upon reasonable request.

652 **REFERENCES**

- 653 Alonso, E.E., Pereira, J.M., Vaunat, J. and Olivella, S., 2010. A microstructurally based effective stress  
654 for unsaturated soils. *Géotechnique*, 60(12), pp.913-925.
- 655 Anandarajah, A. and Yao, M., 2002. Three-dimensional Discrete Element Method of analysis of clays.  
656 In *Discrete Element Methods: Numerical Modeling of Discontinua* (pp. 237-241).
- 657 Andò, E., Hall, S. A., Viggiani, G., Desrues, J., & Bésuelle, P. (2012). Grain-scale experimental  
658 investigation of localised deformation in sand: a discrete particle tracking approach. *Acta Geotechnica*,  
659 7(1), 1-13.
- 660 Arganda-Carreras, I., Kaynig, V., Rueden, C., Eliceiri, K. W., Schindelin, J., Cardona, A., & Sebastian  
661 Seung, H. (2017). Trainable Weka Segmentation: a machine learning tool for microscopy voxel  
662 classification. *Bioinformatics*, 33(15), 2424-2426.
- 663 Cetin, H. and Gökoğlu, A., 2013. Soil structure changes during drained and undrained triaxial shear of  
664 a clayey soil. *Soils and foundations*, 53(5), pp.628-638.
- 665 Chen, Y., Ma, G., Zhou, W., Wei, D., Zhao, Q., Zou, Y. and Grasselli, G., 2021. An enhanced tool for  
666 probing the microscopic behavior of granular materials based on X-ray micro-CT and FDEM.  
667 *Computers and Geotechnics*, 132, p.103974.
- 668 Cheng, Z., & Wang, J. (2018). A particle-tracking method for experimental investigation of kinematics  
669 of sand particles under triaxial compression. *Powder Technology*, 328, 436-451.
- 670 Chevalier, B., Tsutsumi, Y. and Otani, J., 2019. Direct shear behavior of a mixture of sand and tire  
671 chips using X-ray computed tomography and discrete element method. *International Journal of*  
672 *Geosynthetics and Ground Engineering*, 5(2), pp.1-12.
- 673 Druckrey, A. M., & Alshibli, K. A. (2014). 3D behavior of sand particles using X-ray synchrotron  
674 micro-tomography. Paper presented at the Geo-Congress 2014: Geo-characterization and Modeling for  
675 Sustainability.

- 676 Fu, Y., Wang, L., Tumay, M. T., & Li, Q. (2008). Quantification and simulation of particle kinematics  
677 and local strains in granular materials using X-ray tomography imaging and discrete-element method.  
678 *Journal of engineering mechanics*, 134(2), 143-154.
- 679 Haldrup, K., Nielsen, S. F., & Wert, J. A. (2008). A general methodology for full-field plastic strain  
680 measurements using X-ray absorption tomography and internal markers. *Experimental*  
681 *Mechanics*,48(2), 199-211.
- 682 Hall, S. A., Desrues, J., Viggiani, G., Bésuelle, P., & Andò, E. (2012). Experimental characterisation  
683 of (localised) deformation phenomena in granular geomaterials from sample down to inter-and intra-  
684 grain scales. *Procedia Iutam*, 4, 54-65.
- 685 Hall, S.A., Bornert, M., Desrues, J., Pannier, Y., Lenoir, N., Viggiani, G. and Bésuelle, P., 2010.  
686 Discrete and continuum analysis of localised deformation in sand using X-ray  $\mu$ CT and volumetric  
687 digital image correlation. *Géotechnique*, 60(5), pp.315-322.
- 688 Hattab, M., Hammad, T., Fleureau, J.M. and Hicher, P.Y., 2013. Behaviour of a sensitive marine  
689 sediment: microstructural investigation. *Géotechnique*, 63(1), pp.71-84.
- 690 Ibeh, C., Pedrotti, M., Tarantino, A. and Lunn, R., 2019, June. An X-ray CT study of miniature clay  
691 sample preparation techniques. In *E3S Web of Conferences* (Vol. 92).
- 692 Ibeh, C., Pedrotti, M., Tarantino, A. and Lunn, R.J., 2019, May. Initiation and propagation of strain  
693 localization in cohesive soil using a novel miniature triaxial cell and X-ray Computed Tomography. In  
694 *InterPore2019*.
- 695 Karamov, R., Martulli, L.M., Kerschbaum, M., Sergeichev, I., Swolfs, Y. and Lomov, S.V., 2020.  
696 Micro-CT based structure tensor analysis of fibre orientation in random fibre composites versus high-  
697 fidelity fibre identification methods. *Composite Structures*, 235, p.111818.
- 698 Karatza, Z., Andò, E., Papanicolopoulos, S.A., Viggiani, G. and Ooi, J.Y., 2019. Effect of particle  
699 morphology and contacts on particle breakage in a granular assembly studied using X-ray tomography.  
700 *Granular Matter*, 21(3), p.44.
- 701 Kumar, B.S., 2013. Image denoising based on non-local means filter and its method noise thresholding.  
702 *Signal, image and video processing*, 7(6), pp.1211-1227.
- 703 Lin, Z.Y., Wang, Y.S., Tang, C.S., Cheng, Q., Zeng, H., Liu, C. and Shi, B., 2021. Discrete element  
704 modelling of desiccation cracking in thin clay layer under different basal boundary conditions.  
705 *Computers and Geotechnics*, 130, p.103931.
- 706 Madra, A., El Hajj, N. and Benzeggagh, M., 2014. X-ray microtomography applications for quantitative  
707 and qualitative analysis of porosity in woven glass fiber reinforced thermoplastic. *Composites Science*  
708 *and technology*, 95, pp.50-58.
- 709 MATLAB and Statistics Toolbox Release 2020a, The MathWorks, Inc., Natick, Massachusetts, United  
710 States.
- 711 Nielsen, S. F., Poulsen, H. F., Beckmann, F., Thorning, C., & Wert, J. A. (2003). Measurements of  
712 plastic displacement gradient components in three dimensions using marker particles and synchrotron  
713 X-ray absorption microtomography. *Acta Materialia*, 51(8), 2407-2415.
- 714 Pedrotti, M. and Tarantino, A., 2018. An experimental investigation into the micromechanics of non-  
715 active clays. *Géotechnique*, 68(8), pp.666-683.

716 Pedrotti, M. and Tarantino, A., 2019. A conceptual constitutive model unifying slurried (saturated),  
717 compacted (unsaturated) and dry states. *Géotechnique*, 69(3), pp.217-233.

718 Sridharan, A. and Rao, G.V., 1973. Mechanisms controlling volume change of saturated clays and the  
719 role of the effective stress concept. *Geotechnique*, 23(3), pp.359-382.

720 Takemura, T., Oda, M. and Takahashi, M., 2004. Microstructure observation in deformed geomaterials  
721 using microfocus X-ray computed tomography. *X-ray CT for Geomaterials*, pp.299-304.

722 Taylor, H.F., O'Sullivan, C. and Sim, W.W., 2015. A new method to identify void constrictions in  
723 micro-CT images of sand. *Computers and Geotechnics*, 69, pp.279-290.

724 Viggiani, G., Lenoir, N., Bésuelle, P., Di Michiel, M., Marelli, S., Desrues, J. and Kretschmer, M.,  
725 2004. X-ray microtomography for studying localized deformation in fine-grained geomaterials under  
726 triaxial compression. *Comptes Rendus Mécanique*, 332(10), pp.819-826.

727 Zhao, B., Wang, J., Coop, M.R., Viggiani, G. and Jiang, M., 2015. An investigation of single sand  
728 particle fracture using X-ray micro-tomography. *Géotechnique*, 65(8), pp.625-641.  
729

730

731

732

733

734

735

736

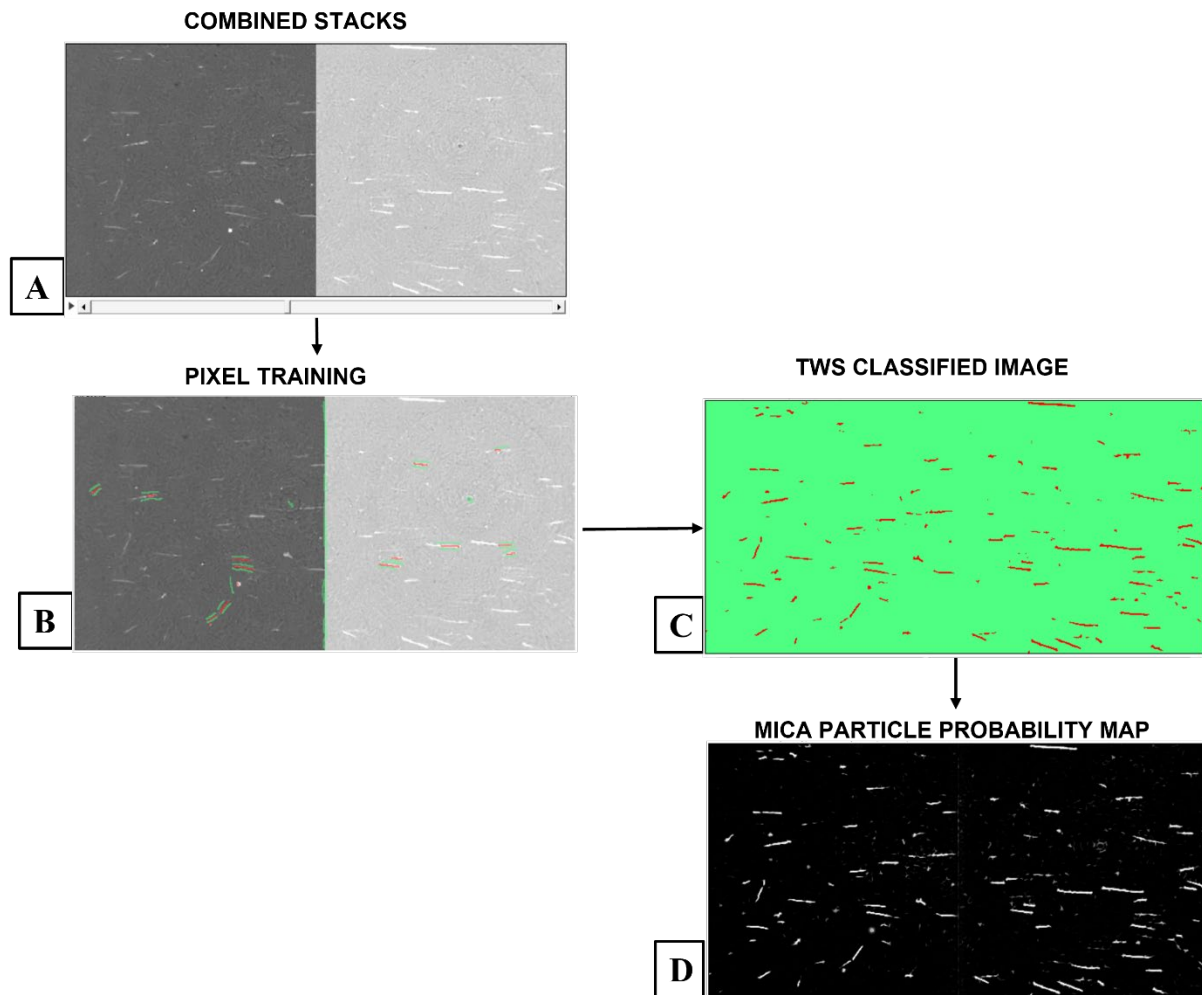
737

738

739

740 Appendix 1

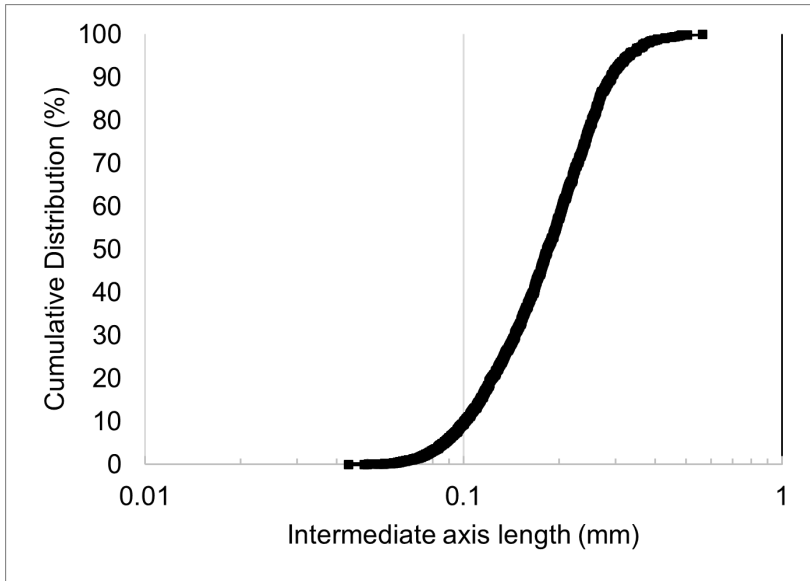
741 Trainable WEKA Segmentation approach



742

743 Figure 18 a) Stacks of CT images used for pixel training, b) pixel training of the stacked image

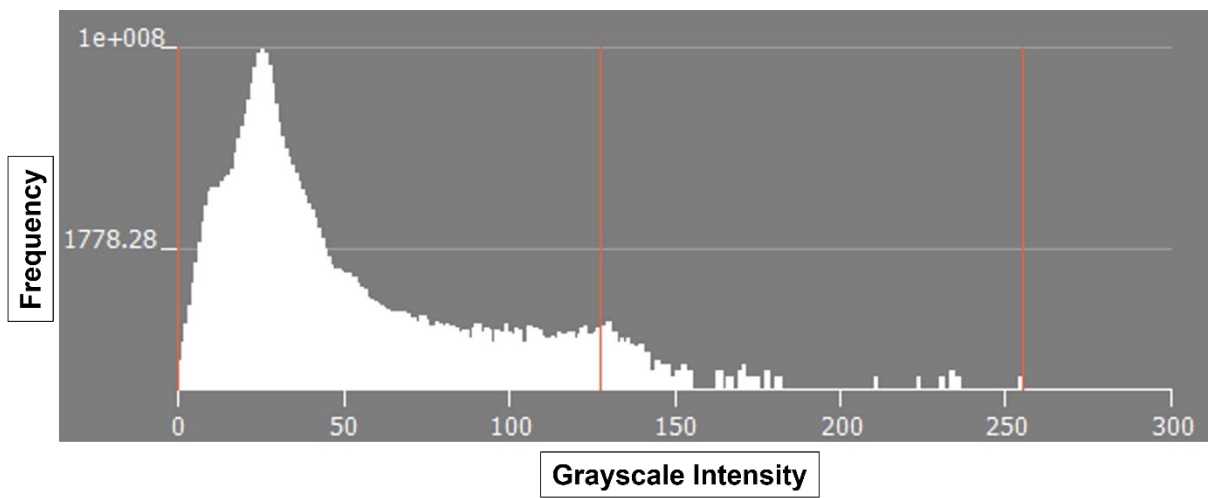
744 c) the stacked CT image classified using TWS d) Mica particles (white section).



745

746 Figure 19: Mica particle cumulative particle intermediate axis length distribution plot.

747



748

749 Figure 20: Greyscale histogram of the imaged sample.